Aeroacoustics Conferences
June 14-17, 2022, Southampton, UK
28th AIAA/CEAS Aeroacoustics 2022 Conference

10.2514/6.2022-3087

Analysis of Spatiospectral Lobes in Installed F404 Engine Noise Radiation

Tyce Olaveson[1] and Jacob A. Ward[2]
Brigham Young University, Provo, Utah, 84602, USA

Jon Paul Johnson[3]
Brigham Young University-Idaho, Rexburg, Idaho, 83440, USA

Kent L. Gee[4]
Brigham Young University, Provo, Utah, 84602, USA

Alan T. Wall[5]
Air Force Research Laboratory, Wright-Patterson AFB, Ohio, 45433

Spatiospectral lobes are still-unexplained phenomena seen in noise radiation from multiple high-performance aircraft. These lobes are observed as multiple peaks in noise spectra at a given field location or as multiple local maxima in noise directivity at a single frequency. Using hybrid beamforming with a 120-microphone near-field array, the lobe characteristics are studied for a GE F404 engine installed on a T-7A aircraft at different engine conditions. Both the measured and reconstructed fields show multiple spatiospectral lobes at different engine conditions, and the overall noise directivity is identified as being the superposition of multiple distinct lobes. The individual lobes appear, shift aft, and then disappear with increasing frequency, which is opposite the behavior of overall noise directivity. The lobes are ray-traced back to the jet centerline to determine an apparent acoustic source location and it is concluded that each lobe originates from a different source within the jet.

I. Nomenclature

AB = Afterburner
C = Cross spectral matrix
D_e = Nozzle exit diameter
G = Free field greens function matrix.
k = Acoustic wave number
L = Regularization matrix
MARP = Microphone Array Reference Point
MIL = Military Power
$\boldsymbol{p}(\boldsymbol{x}_m)$ = Measured pressures at $\boldsymbol{x}_m$, vector

---

[1] Graduate Student, Brigham Young University
[2] Graduate Student, Brigham Young University.
[3] Professor, Department of Physics and Astronomy.
[4] Professor, Department of Physics and Astronomy, AIAA Senior Member.
[5] Research Physicist, Battlespace Acoustics Branch, 2610 Seventh St., Bldg. 441, Wright-Patterson AFB, OH 45433, AIAA member

DCN: 43-9696-22

$\mathbf{Q}_{\mathrm{BF}}$ = Beamforming output
$\boldsymbol{q}(\boldsymbol{x}_s)$ = Source strengths $\boldsymbol{x}_s$, vector
SPL = Sound pressure level
$\boldsymbol{x}_m$ = Microphone positions, vector
$\boldsymbol{x}_s$ = Source location, vector
$\mathbf{W}$ = Weighting matrix
β = Scaling parameter
λ = Regularization parameter
$\Omega(\cdot)$ = Discreet smoothing norm

II. Introduction

Noise fields generated by high-performance military aircraft are of sufficiently high level that repeated exposure, common in the daily routine of nearby personnel, can cause significant hearing loss [1]. Combined with far-field footprints and community annoyance, a more detailed understanding of these noise fields is warranted. Previous studies have used laboratory-scale jets to better characterize the noise fields created by military aircraft (e.g., see [2]). While many conclusions drawn from these experiments have proven useful, there are phenomena present in full-scale military aircraft noise fields that are not present in laboratory studies [3].

One key feature is the presence of multiple spatiospectral lobes that have now been seen in acoustical analyses of several high-performance aircraft [3–11]. These lobes were first identified by Wall et al. [4,5] in their measurements of an installed high-performance military engine with a non-round nozzle. In their paper, total-field reconstructions were created using nearfield acoustical holography, and the lobes were characterized as distinct regions of high sound level. They noted that the lobes evolve through frequency and that the apparent sources of these lobes are distinct. Before this work, the spatiospectral lobes had been identified as being a “dual-peak” phenomenon at individual microphone locations, not a phenomenon connected across space and frequency in a “spatiospectral” sense. These lobes have now been identified using spatiospectral maps [4–6,10]. For example, Wall et al. [7] identified a total of four lobes and speculated that additional lobes may be present but were indistinguishable in their analyses.

Very little evidence has been shown for the presence of spatiospectral lobes in laboratory-scale measurements. Seiner et al. [12] studied spectra collected in the vicinity of a variable temperature jet. From their spectra, a double peak phenomenon can be seen in the high total temperature curves. Another study completed by Long et al.[13] examined jet conditions meant to model runup/takeoff conditions of standard military aircraft. They used acoustical holography to recreate spectra at varying distances from the jet centerline. These spectral maps (see Fig. 9 of Ref [13]) show evidence of spatiospectral lobes.

The underlying mechanics for these lobes are not well understood, though theories have been extended. Wall et al. [5] suggested that the lobes may be related to shock cells. Tam and Parish [14] investigated the possibility of indirect combustion noise from within the nozzle. Lui et al. [15] draw connections between LES simulations and F22A Raptor measurements, suggesting that the “dual-lobe” pattern is related to Mach wave radiation. Differences between Mach wave radiation and large-scale structure noise have also been discussed. However, to further explore the presence of spatiospectral lobes in the F-35, Leete et al. [11] used holography methods to create spatiospectral maps and total field reconstructions. They identified up to five distinct lobes and showed that multiple lobes are present at single frequencies. Through field reconstructions, they showed that the lobes evolve with frequency. At higher frequency, individual lobes shift farther downstream with their apparent source locations moving closer to the engine. Additionally, new lobes appear at steeper angles than the preceding ones.

To improve understanding of the aeroacoustic sources in full-scale military engine jet noise, various methods of source characterization have been explored. As evidenced by the studies of Wall et al. [16] and Leete et al. [11], near-field acoustical holography (NAH) , as well as the statistically optimized variant (SONAH) with multisource extension (M-SONAH), have been used successfully in source characterization on other high-performance aircraft [4,5,7,11,16]**.** Vold et al.[17] also developed a method to decompose jet noise sources into azimuthal modes. In addition to holography methods, beamforming has also been used successfully as a method of acoustical source characterization [8,18,19]. Finally, vector acoustic intensity methods have been used for direct measurements of the sound power flux in the radiated field [9,20].

Because of its advantages in eventually creating reduced-order wavepacket models [21], an advanced beamforming method has been selected for the study of the spatiospectral lobe phenomenon. Padois et al. [22] proposed an alternative to conventional beamforming and other advanced methods called the hybrid beamforming method (Hybrid Method). Instead of following the standard delay-and-sum technique seen in conventional beamforming, the Hybrid Method solves the inverse problem through regularization methods and solves for all sources simultaneously. The result is an equivalent source model (ESM) that consists of a line (or other arrangements) of complex monopoles, that gives both phase and amplitude information and embeds partial source coherence as a function of frequency. This method has been successfully applied to other aeroacoustic sources [19,23].

This paper makes use of the Hybrid Method to calculate an ESM for the sound field generated by a GE F404-103 (hereafter abbreviated to F404) engine installed on the Boeing/Saab T-7A "Red Hawk". The model is then used to create total field reconstructions, where the spatiospectral lobes can then be studied. Related to Leete et al. [11], ray tracing techniques are used to identify trends in lobe evolution, which yield results qualitatively consistent with previous experiments but at higher resolution. For supersonic engine powers, it is concluded that each lobe originates within discrete source regions.

III. Measurements

On August 18th, 2019, acoustical data were collected from a tied-down T-7A aircraft at Holloman Air Force Base. The measurement process, explained more extensively in Ref. [10], included over 200 microphones. These microphones were arranged to record data in the near and far-fields. The microphones were arranged in arrays to take measurements within the immediate vicinity of the aircraft out to 750 ft. The aircraft was taken through a series of six run-ups where the aircraft was cycled through various engine powers, including military power (MIL) and afterburner (AB).

This paper uses the data collected from a 120-microphone imaging array. This array (shown in Fig. 1) linearly followed the approximate shear layer downstream of the aircraft, then ran along the aircraft at the minimum distance allowed in keeping with hazard zones. This array was spaced non-uniformly with microphones closer together near the aircraft and farther apart downstream. Unlike prior imaging measurements that used uniform spacing, the arrangement was designed to best capture the expected frequency content in each of these regions and maximize overall bandwidth with the number of microphones available. The data were collected at a sampling rate of 204.8 kHz and with a recording length of 30 seconds for each run-up. The complex pressures from all six runups were concatenated to allow for an averaged cross spectral matrix. Data block length was chosen such that the spectral data has a frequency resolution of 3 Hz. This balances frequency resolution with the number of blocks available for averaging.

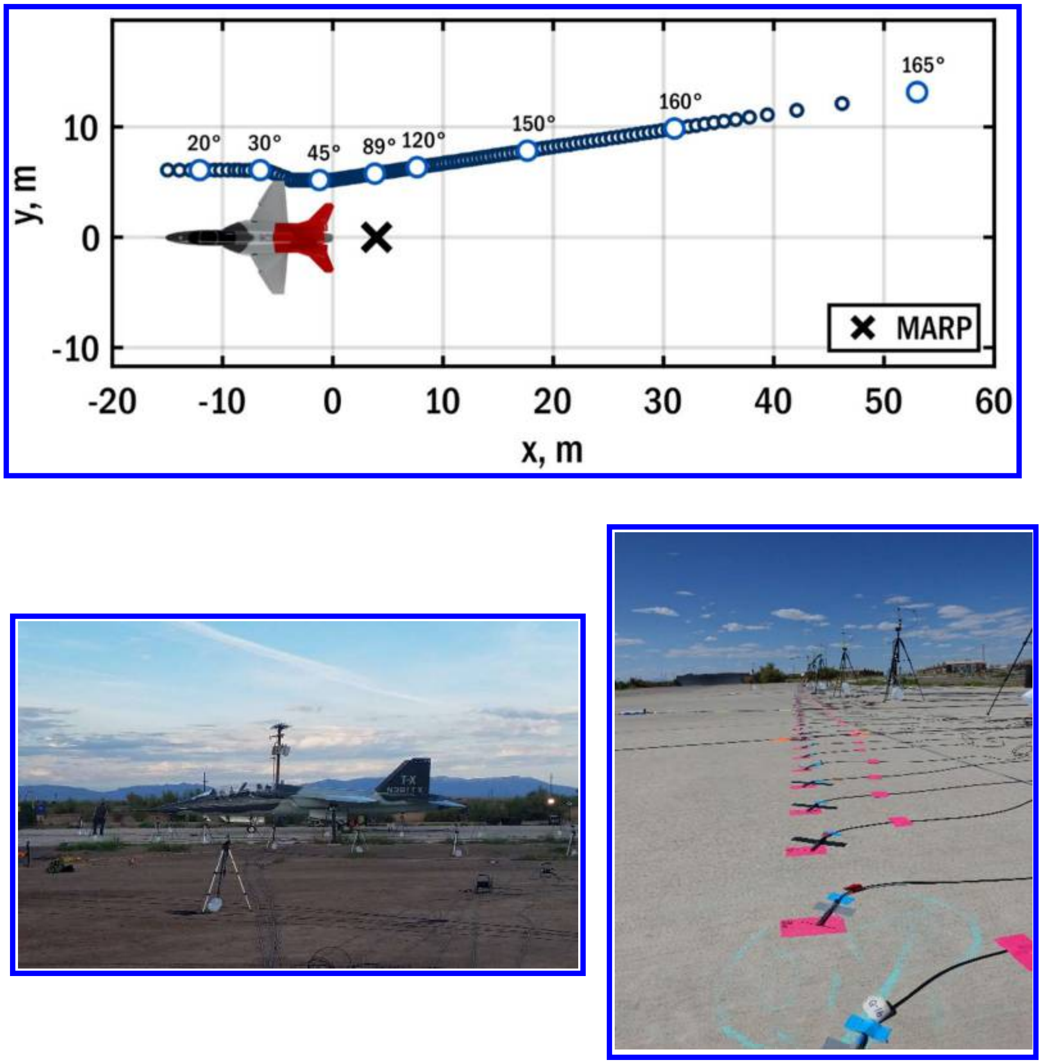

Fig. 1. Top. Schematic of the 120-microphone imaging array used for the analyses of this paper. Bottom. Images of the physical setup. On the left is the aircraft with microphones from different arrays seen on tripods. On the right, the microphones forming the imaging array are seen taped to the concrete runway.

After the initial measurements were recorded, spatiospectral maps were generated for four engine conditions: 50% thrust, 75% thrust, MIL, and AB. These are shown in figure 2. Each map shows the spectra as a function of position. Colors indicate the sound pressure level at each point. A distinct lobing behavior is also seen at each engine condition these are the spatiospectral lobes. At lower engine powers there are fewer lobes with two at 50% thrust and up to four at 75% thrust. At the higher engine powers, five or more are seen. At AB conditions the lobes are less distinct, and the higher-ordered lobes can be seen to merge. This feature was noted by Hales et al. [24] who showed that the lobes flattened and merged, resulting in a smaller coherence length. Similar behavior can be seen in the spatiospectral maps produced by Leete et al. [11].

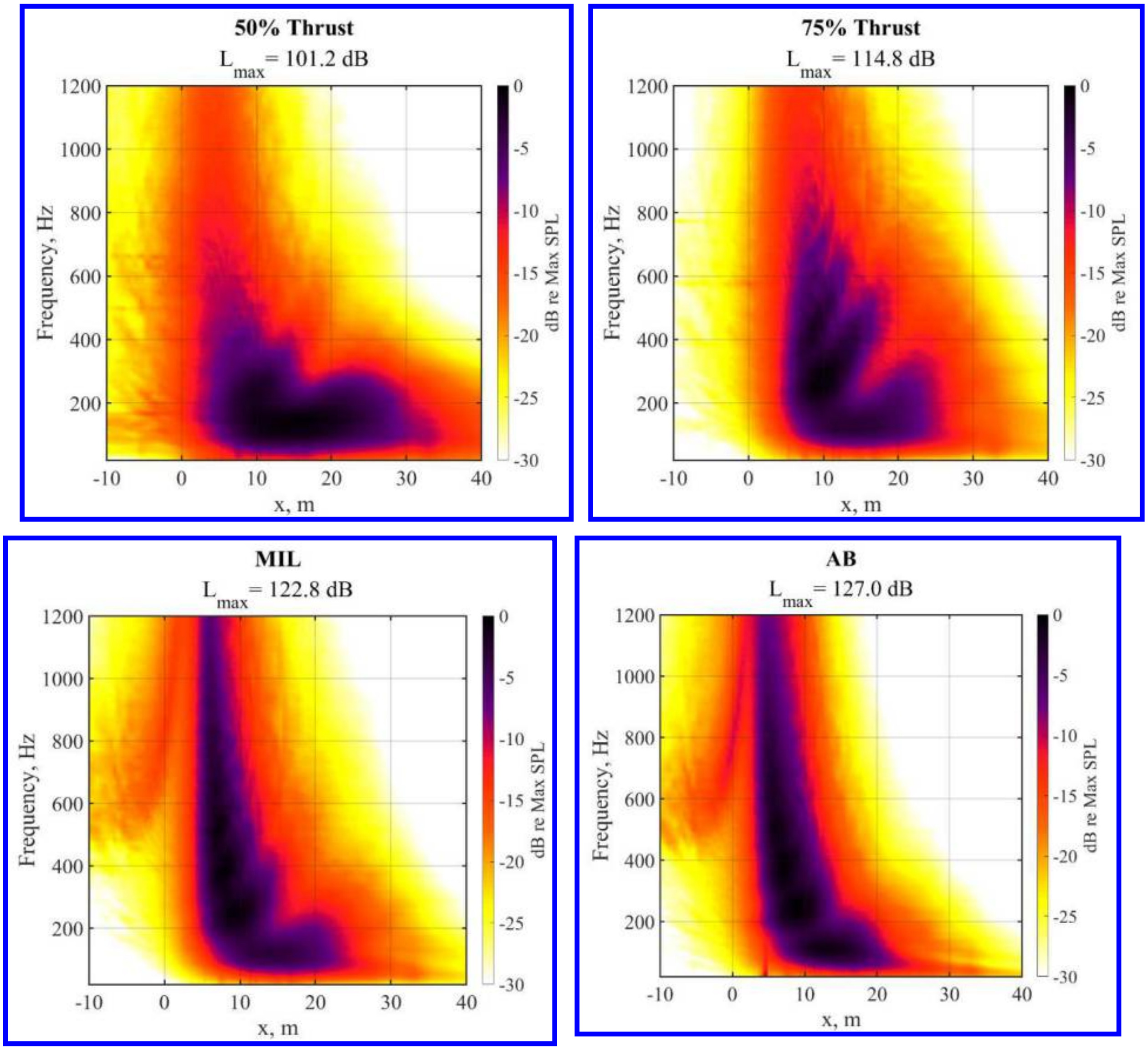

Fig. 2 Spatiospectral maps produced from the T7A measured spectra. Four engine conditions are included and the spatiospectral lobes can be seen as regions of local maxima in the central region. ***[Will add numbers later to identify the lobes].***

IV. Methods

In attempting to explore spatial lobe characteristics, certain limitations are quickly manifest. Data are measured at 120 field locations along the imaging array, but with much coarser spatial resolution elsewhere. Attempting to perform an analysis with only these data points will produce results with limited resolution. Since it was unreasonable to attempt to record the field at every possible location desired for analysis of the spatiospectral lobe phenomenon, the strategy is to use the Hybrid Method to reconstruct a field with a fine resolution. Using the information collected at the imaging array and assuming a reflection-free environment, the Hybrid Method is used to construct an ESM. The ESM can then be used to project the data from the imaging array to any field location, providing sufficient resolution to study the spatiospectral lobes. Leete et al. employed the same basic strategy for a spatiospectral lobe analysis of the F-35 but using M-SONAH. The Hybrid Method was used here in part to see if there were any particular advantages in applying one method over another in producing a fine reconstruction, a question that has not been yet explored. This section highlights the important aspects of the derivation of the Hybrid Method. See reference [22] for a more in-depth derivation.

A. General Problem

The general idea of beamforming is to solve the inverse problem that relates the source strengths to the pressures. In matrix form, this is written as

$$\mathbf{p}(\boldsymbol{x}_m) = \mathbf{G}(\boldsymbol{x}_m, \boldsymbol{x}_s)\mathbf{q}(\boldsymbol{x}_s), \tag{1}$$

where $\boldsymbol{p}(\boldsymbol{x}_m)$ is a vector containing the recorded pressures at the microphone array, $\boldsymbol{q}(\boldsymbol{x}_s)$ is a vector containing the (unknown) source strengths and

$$\mathbf{G}(\mathbf{x_m}, \mathbf{x_s}) = \frac{1}{4\pi\|\mathbf{x_m} - \mathbf{x_s}\|} e^{-jk\|\mathbf{x_m} - \mathbf{x_s}\|} \tag{2}$$

is the free field Green's function that mathematically describes the acoustic propagation from the sources to the microphones.

One method of solving this problem is to reformulate Eq. 1 in terms of the equivalent minimization problem:

$$\mathbf{q}_{\lambda\beta} = \operatorname{argmin}\|\beta\mathbf{p} - \mathbf{Gq}\|_2^2 + \lambda^2\Omega(\mathbf{q}), \tag{3}$$

where $\Omega(\cdot)$ is a discrete smoothing norm, λ a regularization parameter and $\|\cdot\|_2$ denotes the vector 2-norm. The scaling parameter β is also introduced to reduce possible overregularization caused by λ. The purpose of the smoothing norm is to reduce the impact of measurement noise on the inverse method. The smoothing norm can be defined as

$$\Omega(\mathbf{q}) = \|\mathbf{Lq}\|_2, \tag{4}$$

where $\mathbf{L}$ is a square regularization matrix and is chosen differently depending on which method is used to solve the problem. The solution can then be found by setting the derivative of the cost function (Eq. 2) equal to zero. Padois et al. [22] calculate the solution as

$$\mathbf{q}_{\lambda\beta} = \mathbf{L}^{-1}([\mathbf{L}^{-1}]^{\mathrm{T}}\mathbf{G}^{\mathrm{H}}\mathbf{G}\mathbf{L}^{-1} + \lambda^2\mathbf{I})^{-1}[\mathbf{L}^{-1}]^{\mathrm{T}}\mathbf{G}^{\mathrm{H}}\beta\mathbf{p}, \tag{5}$$

where $(\cdot)^T$ denotes a matrix transpose and $(\cdot)^H$ the Hermitian transpose. By making a few substitutions, Eq. 4 can be related to the standard form of the inverse problem.

$$\mathbf{q}_{\lambda\beta} = \mathbf{L}^{-1}\underline{\mathbf{q}}_{\lambda\beta} = \mathbf{L}^{-1}\left(\underline{\mathbf{G}^{\mathrm{H}}}\,\underline{\mathbf{G}} + \lambda^2\mathbf{I}\right)^{-1}\underline{\mathbf{G}^{\mathrm{H}}}\beta\mathbf{p}\,, \tag{6}$$

where $\underline{\mathbf{G}} = \mathbf{G}\mathbf{L}^{-1}$ is the steering vector. The difference between these two formats is that the solution $\underline{\mathbf{q}}_{\lambda\beta}$ can be thought of as a regularized inverse problem, whereas $\mathbf{q}_{\lambda\beta}$ is both regularized and scaled. With the problem outlined, the Hybrid Method is now developed to solve Eq 5.

B. Hybrid Method

The Hybrid Method solves the problem by choosing a smoothing norm and other regularization parameters according to how the system responds to standard beamforming processing. This is done by defining a beamforming output $\mathbf{Q}_{\mathrm{BF}} = \mathbf{W}^{\mathrm{H}}\mathbf{C}\mathbf{W}$, where $\mathbf{W}$ is a weighting matrix and $\mathbf{C} = \mathbf{p}\mathbf{p}^{\mathrm{H}}$ is the cross spectral matrix (CSM). The weight matrix has elements defined as $W_{ij} = G_{ij}/\mathbf{g}_{\mathrm{j}}^{\mathrm{H}}\mathbf{g}_{\mathrm{j}}$ where $\mathbf{g}_{\mathrm{j}}$ is the j$^{\mathrm{th}}$ column of $\mathbf{G}$.

The regularization matrix is now defined as

$$\mathbf{L}^{-1} = \left[\operatorname{diag}\left(\frac{\sqrt{\operatorname{Diag}(\mathbf{Q}_{\mathrm{BF}})}}{\sqrt{\|\operatorname{Diag}(\mathbf{Q}_{\mathrm{BF}})\|_\infty}}\right)\right], \tag{7}$$

where $\mathrm{diag}(\mathbf{V})$ maps the vector $\mathbf{V}$ onto the main diagonal of a square matrix, $\mathrm{Diag}(\mathbf{M})$ is a vector composed of the diagonal elements of the matrix $\mathbf{M}$ and $\|\cdot\|_\infty$ denotes the infinity norm. Due to the normalization in the denominator, $\mathbf{L}^{-1}$ is now bounded between 0 and 1.

Since the beamforming output is defined in terms of the CSM, the solution must also be converted into a similar form. This is done by defining the source matrix as $\mathbf{Q}_{\lambda\beta} = \mathbf{q}_{\lambda\beta}\mathbf{q}_{\lambda\beta}^{\mathrm{H}}$. Reformulating Eq. 5 accordingly, the solution is found as

$$\mathbf{Q}_{\lambda\beta} = \mathbf{L}^{-1}\,\underline{\mathbf{Q}}_{\lambda\beta}\,(\mathbf{L}^{-1})^{\mathrm{H}} = \mathbf{L}^{-1}\beta\big(\mathbf{J}_\lambda\,\underline{\mathbf{G}^{\mathrm{H}}}\big)\,\mathbf{C}\,\big(\underline{\mathbf{G}}\,\mathbf{J}_\lambda^{\mathrm{H}}\big)\beta^{\mathrm{H}}\,(\mathbf{L}^{-1})^{\mathrm{H}}, \tag{8}$$

where, for simplicity, $\mathbf{J}_\lambda$ has been introduced:

$$\mathbf{J}_\lambda = \left(\underline{\mathbf{G}^{\mathrm{H}}}\,\underline{\mathbf{G}} + \lambda^2\mathbf{I}\right)^{-1}, \tag{9}$$

At this point everything in Eq. 7 can be either computed or measured, except for the parameters λ and β. The purpose of the scaling parameter β is to compensate for the effect of a uniform addition of λ^2 in the $\mathbf{J}_\lambda$ term. For this reason, Ref. [22] defines the scaling parameter as $\beta = \left\|\underline{\mathbf{G}^{\mathrm{H}}}\,\underline{\mathbf{G}} + \lambda^2\mathbf{I}\right\|_2$ and shows that the optimal value for λ is 5% of the maximum eigenvalue of the $\underline{\mathbf{G}^{\mathrm{H}}}\,\underline{\mathbf{G}}$ matrix squared. Further explanation of the intricacies of this method can be found in Ref. [22].

Now that a (relatively) clean method is available, the measurements described in section III can be used to numerically evaluate Eq. 7 and create an equivalent source model.

With an equivalent source model, the sources are iteratively radiated out to any point of interest via Rayleigh integrals. An appropriate density is thus required for the desired resolution. In this paper, a density of roughly 18 points per square meter is used which allows the curvature of the spatiospectral lobes to be clearly visible over the spatial and frequency range of interest.

C. Ray Tracing

As part of the spatiospectral lobe analysis, ray tracing methods are employed (see section V.B). This section gives a brief explanation of the ray-tracing methodology.

Once the Hybrid Method has been used to construct an ESM for a given frequency, the sources are propagated out to the desired field points. The field reconstruction is then decomposed into polar coordinates, r and θ, with $r = 0$ at the MARP and $\theta = 0$ towards the front of the aircraft. From here, discrete concentric arcs of constant r are programmatically searched for local maxima in SPL. The result is a series of points that can then be fit to a linear curve (see Fig 3) and from the fit parameters propagation angle and jet line intercept can be extracted. In the end, the fit is visually verified to be accurate.

Some frequencies exhibit multi-lobe behavior and thus require additional consideration. For these fields the process is the same as for the single-lobe case. The concentric arcs are searched for local maxima in SPL and multiple values are sometimes returned. In these cases, a few criteria are used to determine if the point belongs to a lobe or not. It is observed that spatiospectral lobes tied to turbulent mixing noise are seen only downstream of the engine nozzle exit, thus local maxima in the upstream direction ($\theta < 90°$) are ignored. Additionally, if relatively few local maxima are found to lie along a lobe, that lobe is ignored. The effect is that new lobes are ignored until they become distinctly separate, and old lobes vanish as their structure is absorbed into the other.

Figure 3 illustrates the basic methodology presented above. The calculated total field reconstruction is greyed out and dark arcs represent the regions searched for local maxima. Sample maxima are identified by black points and the raytraced fits are included as colored lines. Note that these points visually lie within each lobe, but not perfectly on the linear fits. This is to be expected. This novel approach provides a faster and more rigorous method for identifying the lobes over that of Leete et al. [11], who used a similar method for programmatically identifying the local maxima but then the curves were manually fit visually. The result here is the ability to perform the ray tracing significantly faster and more accurately. Thus, the results in this paper have less scatter and greater frequency resolution than those in Ref. [11].

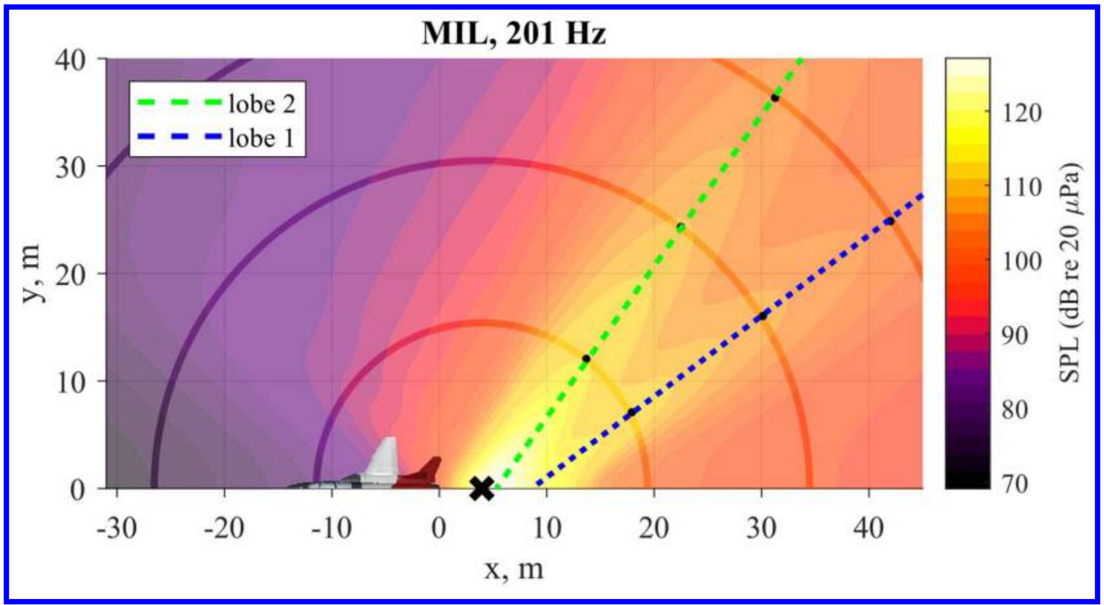

Fig. 3. Diagram of ray tracing methodology. Dark arcs represent areas where the program is searching for local maxima. Black points indicate where the script has identified a local maximum and the black X is the MARP location. Only three arcs are presented in this figure. In practice, the field reconstruction is discretized into many concentric arcs, and each is searched for local maxima providing hundreds of points to curve fit.

V. Results

A. Total Field Reconstructions

The stated objective of this paper is to use the additional resolution from the Hybrid Method-reconstructed field to study the spatial characteristics of the lobes. Understanding these field characteristics is part of understanding requirements for source models to capture the relevant physics. Using the Hybrid Method and the sound measurements taken from the imaging array, equivalent source models are calculated for four engine conditions at frequencies between 3 and 500 Hz. Above these frequencies, spatial aliasing introduces grating lobes into the field reconstructions. Each ESM is then propagated outward to determine near-field sound levels to the side of the aircraft. Methods such as UPAINT [4] use an interpolation with phase unwrapping to increase the spatial Nyquist frequency. These methods will be implemented in future work to explore higher frequencies.

The total-field reconstructions seen in Fig. 4 allow easy identification of example spatiospectral lobes from 50% thrust through AB. Each figure presents an overhead view of the T-7A and sideline area. The *x* axis gives the distance (in meters) downstream of the nozzle and the *y* axis gives the distances to the side of the aircraft relative to the centerline. An overlaid colormap represents the sound level at each field location and is referenced to the maximum SPL in the reconstructed region, included in the corresponding header. In each figure, the sound is seen to primarily radiate at a downstream angle, as expected. The two frequencies shown, 81 Hz and 171 Hz, have been selected to demonstrate characteristic behavior. At frequencies less than ~150 Hz for all engine conditions, the radiation is dominated by a single region (Fig. 4 a, c, e, and f). At some higher frequencies, the radiation is seen to be composed of multiple lobes (Fig. 4 b, d, f, and h), two at a time. This can be seen by examining the variation in sound level in Fig. 2 across downstream distance for different constant frequencies. Note that the frequencies where new lobes appear also exhibit a semi-harmonic pattern that is likely physically significant. By cycling through frequency, visual patterns manifest themselves and lobe characteristics are identified.

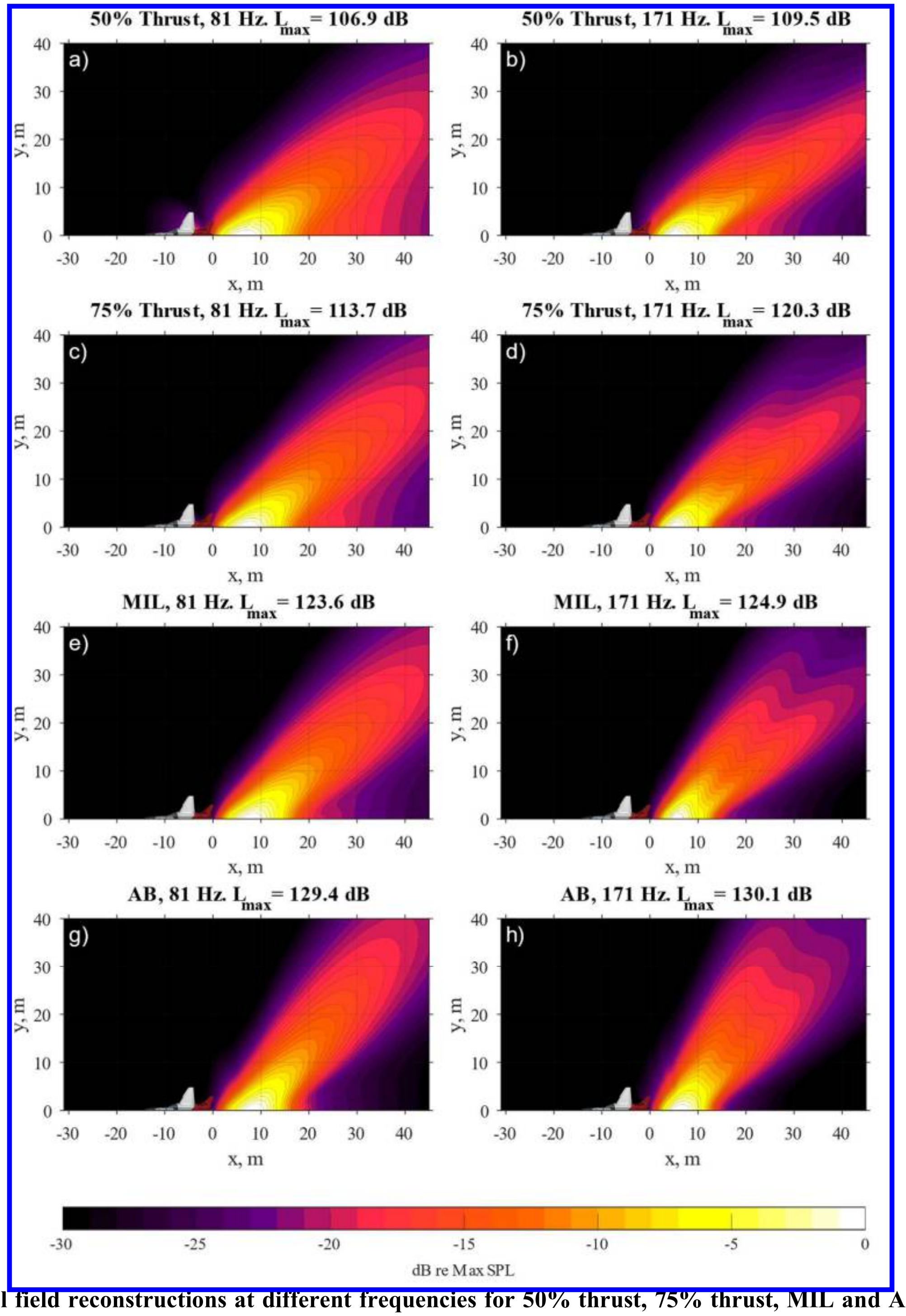

Fig. 4 Total field reconstructions at different frequencies for 50% thrust, 75% thrust, MIL and AB engine conditions. These plots were chosen to illustrate the appearance of the spatiospectral lobes.

B. Linear Fits

While trends of the lobes can be visually identified, the more rigorous approach described in section III.C is used to quantify these properties. For every field reconstruction, the lobes are raytraced according to the process in section III.C. The linear fit parameters are then extracted and used to calculate the approximate jet centerline intercept and radiation angle.

Examples of these fits are provided in Fig 5. Each image shows the associated field reconstruction, now with SPL in dB re 20 μPa, and the linear fit(s) for each frequency. The lobes are color coded with the first being blue, the second green, the third red and the fourth (not shown) cyan. In the header, the calculated jet centerline intercepts and radiation angles are reported. The frequencies presented here were chosen to better illustrate the behavior of the lobes between engine conditions. On the left, reconstructions are made at 129 Hz where only a single lobe is present. On the right, reconstructions are made at 333 Hz where two lobes are present in most cases. It is important to note that when multiple spatiospectral lobes are present, they are not artificially forced to the same centerline intercept. Additionally, the same lobes do not appear at the same frequencies for all engine conditions (compare 50% Thrust to AB).

Using the x-intercepts and angles from the ray traced plots, overall trends are plotted in Fig. 6 to help quantitatively identify the lobe properties. Here, frequency is plotted on the y-axis and intercepts (left) or directivity angle (right) along the x-axis. As in Fig. 5, each lobe is color coded and engine power increases from top to bottom.

From the directivity trends the individuality of each lobe can be seen as there is no angle overlap between the lobes for these observations. This is further supported by coherence analysis performed Wall et al. [4] who showed that the lobes are self-coherent, but mutually incoherent. It is also noted that as frequency increases, each individual lobe shifts farther upstream. In addition, new lobes appear at steeper angles than the preceding ones.

The intercept trends give insights into the apparent source locations. As frequency increases, the intercepts for each lobe move closer to the engine. New lobes also appear farther upstream than previous lobes. From their analysis on the F-35, Leete et al. [11] observed that individual lobes sweep aft with increasing frequency until they leave the array aperture, and new lobes appear upstream and swing aft. Similar behavior is seen in this paper, but the increased resolution presented here enhances Leete et al.'s explanation. While individual lobes swing aft with increasing frequency, many lobes (especially Lobe 1) initially move forward and then swing aft as the second lobe gains prominence. An additional observation is that while new lobes appear upstream of the preceding lobes, they quickly move upstream and remain in a relatively fixed location.

It must also be noted that for the 50% and 75% thrust engine conditions combinations of numerical aliasing and the close angular proximity between lobes caused the ray tracing method to perform unreliably at frequencies above 400 Hz. For this reason, data are restricted to below 400 Hz. Additionally, this method struggles to consistently separate two lobes when one dominates the other. The result is a discontinuity in the intercept trends at the transition between two lobes. Visual analysis of these frequencies suggests a smooth and continuous transition, revealing a limitation of the ray tracing technique used.

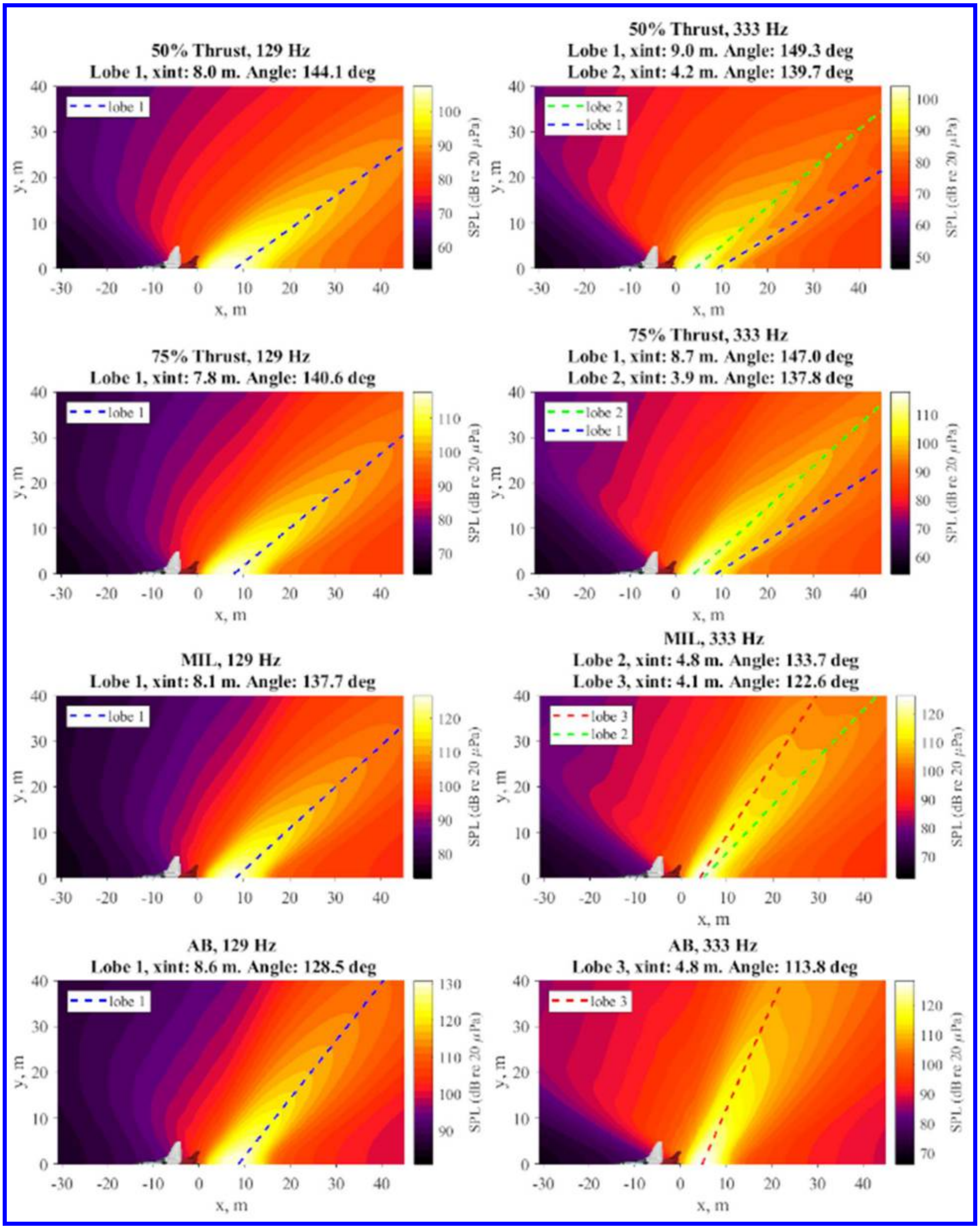

Fig. 5 Examples of ray-traced spatiospectral lobes for four engine conditions. On the left, 129 Hz is chosen to show a single lobe at all powers. On the right, 333 Hz is chosen to show instances of multiple spatiospectral lobes and to show differences between engine conditions. Engine power increases from top to bottom.

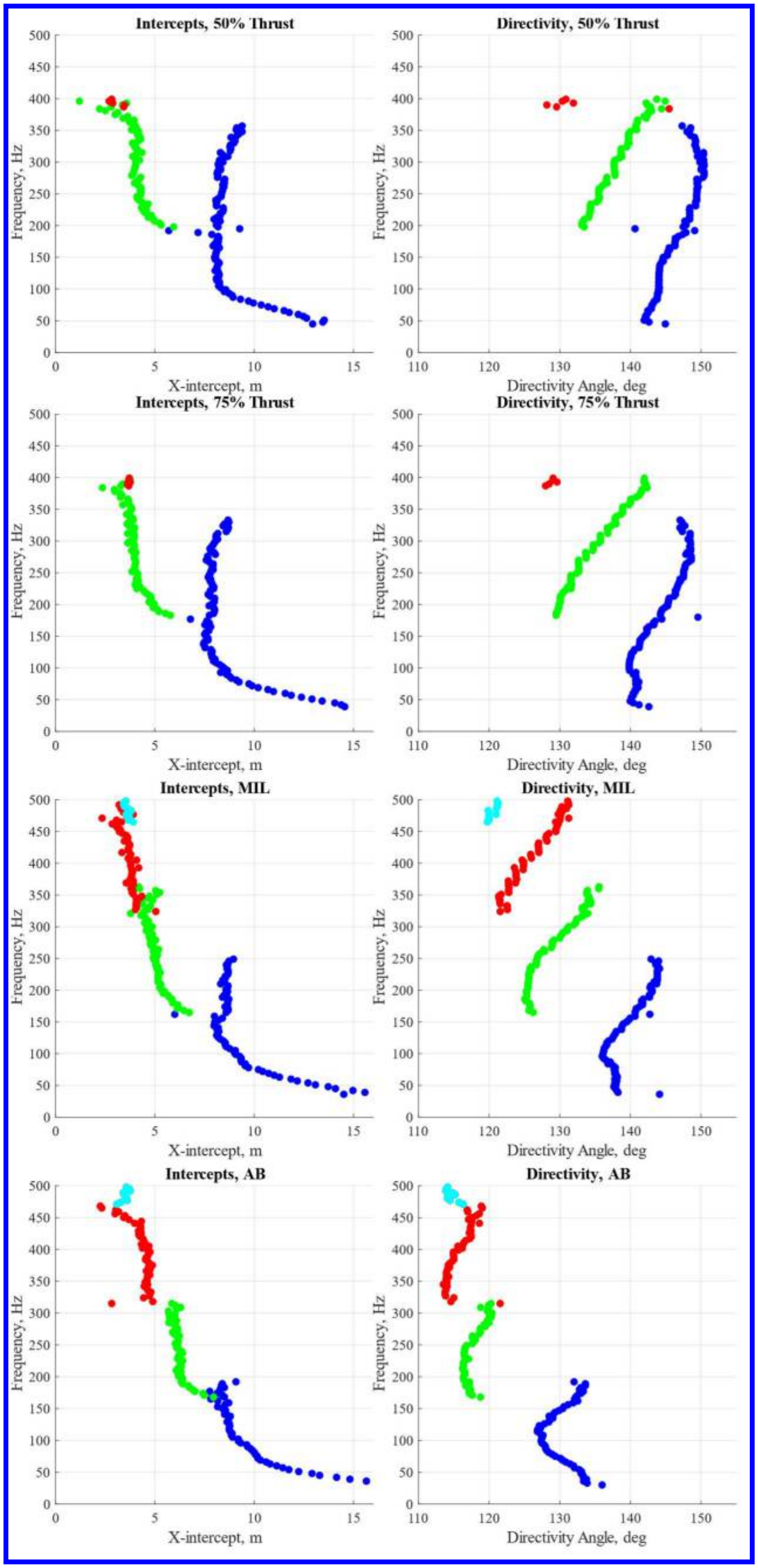

Fig. 6 Directivity and intercept trends seen for four engine conditions. Left: jet centerline intercepts for each lobe. Right: radiation angle for each lobe. Engine power increases from top to bottom.

C. Source Characteristics

It is interesting to note the discrete lobe transitions visible in the intercept trends. Between the four engine conditions, two are identified. The first is clearly visible at roughly 8 m downstream as a division between Lobes 1 and 2. The second is slightly below 5 m at the transition between Lobes 2 and 3. This is more clearly seen in the MIL and AB conditions as Lobe 3 is not fully realized in this frequency range of the lower engine powers. With these transitions occurring at discrete locations, it is possible that the individual lobes can be connected to different flow regions in the jet.

Leete et al. [25] studied noise radiation properties from a large-eddy simulation of a highly heated, imperfectly expanded jet performed by Liu et al. [15,26,27]. With a TTR of 7 and a supersonic Mach number of 3.38 the LES was meant to mimic afterburner conditions. In their analysis they tied noise radiation to different flow regimes defined by the potential core tip at 7.2 nozzle exit diameters, D_e, and the supersonic core tip at 12.7 D_e. Although spatiospectral lobe phenomena were only weakly seen in that analysis, these characteristic lengths (of ~7 and ~13 D_e) are applied to further interpretation of the results in Fig. 6.

From analyzing photographs of the static measurements, the T-7A-installed F404 nozzle has a nozzle exit diameter of ~0.6 m at AB. A calculation for the potential and supersonic core distances for the F404 at AB indicates that the potential core is likely to extend out to 4-4.5 m, and the supersonic core to 7.5-8.0 m. Within 1 D_e, these values are approximately where discontinuities are seen in the Fig 6. intercept trend for both MIL and AB. The transitions in the intercept trends imply that each lobe is coming from a distinct region within the jet and that the lobes are tied to different noise phenomena related to these different flow regions corresponding to the approximate locations of the potential and supersonic core tips. A concurrent analysis by Mathews et al. [28] used nearfield acoustical holography to investigate the source characteristics of this same experiment. In their work, spatiospectral plots (like those in Fig. 2) were produced using reconstructions at the nozzle lipline for AB. They identified three local maxima and placed their locations at around 7.3 m (maximum I), 5.1 m (maximum II), and 4.2 m (maximum III). Equating the Lobes in this paper to the maxima in their paper, the source locations are consistent to within half a meter.

At afterburning conditions, Lobe 1 seems to originate at or downstream of the supersonic core tip below ~150 Hz. The average directivity angle is roughly 130°. Lobe 2 comes from within the supersonic core downstream of the potential core tip, with an average radiation angle is about 118°. This lobe begins close to the supersonic core tip, but drifts upstream and remains near the potential core tip. Finally, Lobe 3 comes from upstream of the potential core tip and has a radiation angle of about 116°. These three lobes combine to produce an OASPL lobe of about 120° [10], suggesting that Lobe 2 dominates the overall radiation and that the maximum source region is between the potential and supersonic core tips, in keeping with other supersonic jet noise literature (for example [29]).

In Fig 2 additional lobes can be identified that are not included here. The fourth lobe appears briefly in the MIL and AB trends of Fig 6 while the other lobes appear at frequencies above 500 Hz. The trends calculated here suggest that higher-ordered lobes will have their source upstream of the potential core tip and at steeper angles. These higher order lobes all radiate in approximately the same direction and originate from within the potential core, this points to Mach wave radiation as being the cause of these lobes. It is also important to note that the number of lobes appears to increase as the jet becomes supersonic.

One concern with this explanation is that it does not account for similar patterns for lower engine powers. At 75% thrust, the jet has not yet become supersonic and therefore does not have a fully developed supersonic core. Yet, both 75% and 50% thrust exhibit strong discontinuities at around 8 m downstream. This draws attention to lobe 1.

D. Lobe 1 Analysis

A helpful tool in exploring the cause of Lobe 1 is the event-based beamforming by Vaughn et al. [30]. In their analysis, time domain events are raytraced to an apparent source region and divided into groups and classified. Comparing the directivity and intercept trends to their results, Lobe 1 falls within the green grouping. This group is identified as large-scale turbulence noise (LSN); however, it is possible that this region could correspond to a transition region between Mach waves and LSN. This is also in line with studies by Leete et al. [11] and Swift et al. [24] who suggested that Lobe 1 was a superposition of two noise sources. This explanation also struggles to explain the behavior of Lobe 1 at 50% thrust, since subsonic jets do not radiate Mach waves.

When looking at Lobe 1 between the different engine conditions, a major difference is the longevity of the lobe. At the subsonic engine conditions (50% and 75% thrust) lobe 1 exists up to around 350 Hz, whereas at MIL and AB the lobe decays by 250 and 200 Hz respectively. By comparing the field reconstructions at 300 Hz for all engine conditions (see Fig. 7) a curious phenomenon can be seen. At 50% thrust (Fig. 7a), Lobe 1 is a dominant noise component of comparable SPL to Lobe 2. At 75% thrust (Fig. 7b) Lobe 1 is still a major part of the noise radiation but is at a lower level than Lobe 2 At MIL (Fig. 7c) Lobe 3 is beginning to appear and faint remnants of Lobe 1 can be seen beneath Lobe 2. At AB (Fig. 7d), Lobes 2 and 3 have merged and evidence of Lobe 1 can only be seen as a slight fluctuation in the side contours.

In these same plots SPL increases with engine power, as expected; however, it seems as though Lobe 1 remains at a relatively constant level. There appears to be perhaps a 10 dB increase from 50% to 75% thrust and then no increase between the other engine powers. The result is that Lobe 1 becomes swallowed by the radiation lobes as engine power increases and finally becomes irrelevant by AB.

A similar saturation effect can be seen in the far field directivity of Christian et al. [31] for this same measurement. In their paper, frequency dependent SPL curves are plotted to show how directivity trends change through frequency and engine conditions. At 80 Hz and above, the primary radiation lobe (around 150°) can be seen to increases linearly uniformly in level from 50% to 75% thrust. The transitions to MIL and AB reveal evidence of saturation in the primary radiation angle, seen as slight to no increase in level for certain regions of the curve. This is particularly evident in their 315 Hz curve, where a double peak is clearly seen at 50% thrust and eventually disappears for higher engine powers.

One addition to the above discussion is the possibility of scrubbing noise, i.e., the interaction of the plume with a rigid ground. This explanation could help give some form to the discrepancies between engine conditions above 200 Hz. This type of noise would originate from the impingement point of the plume with the ground. Assuming the plume spreads linearly, the spreading angle required to impinge at a distance x can be calculated as

$$\theta = \arctan\left(\frac{h - d/2}{x}\right) \tag{10}$$

where h is the distance from the ground to the nozzle centerline and d is the nozzle diameter. For afterburning conditions, a spreading angle of 9.5° is required to impinge at 8 m downstream. Moreover, to maintain this same impingement point at lower engine powers, this angle must increase by as much as a degree.

Another possible reason for Lobe 1's behavior could be found in ground reflections interacting with the plume, though further research would be required to explore this possibility.

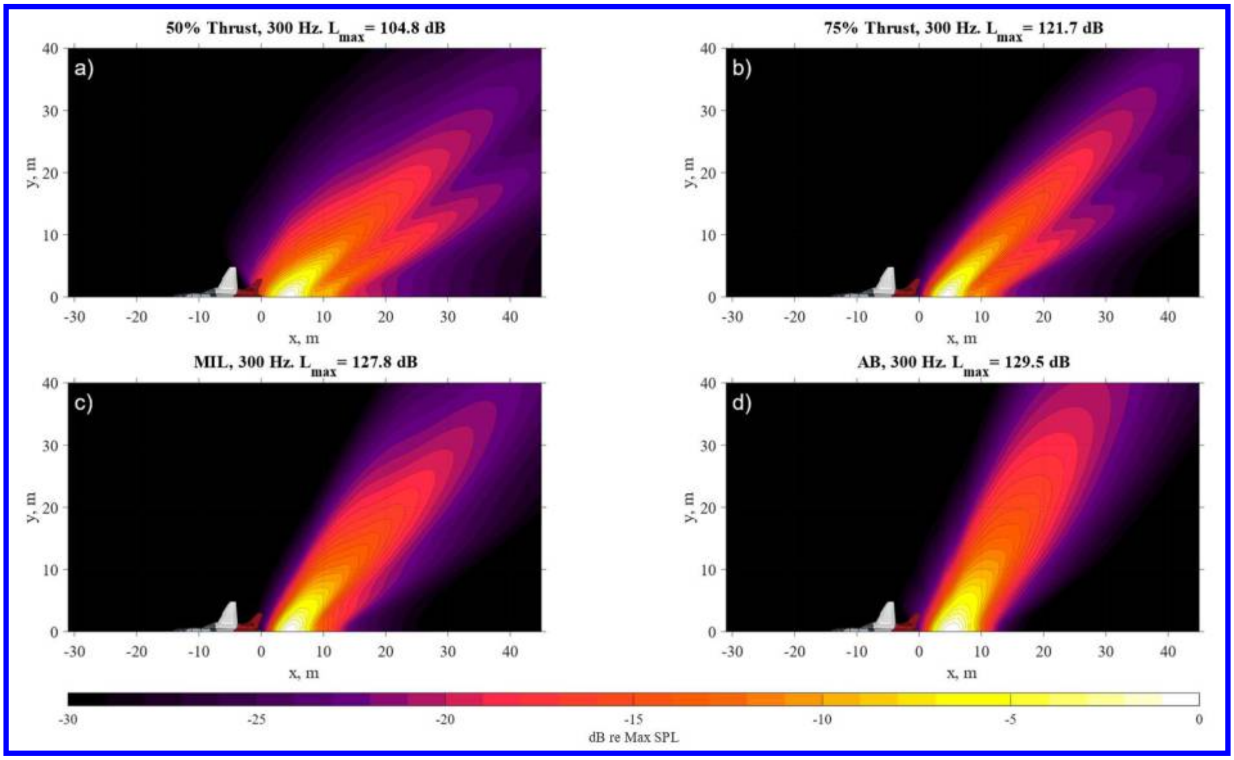

Fig. 7. Field reconstructions at 300 Hz for all four engine conditions. These plots show the behavior of lobe 1 through the different engine conditions. Lobe 1 can be seen on the downstream side of the main radiation lobe. Note that the lobe becomes less prominent with increasing engine power until it is indiscernible at AB.

Conclusion

Near-field sound radiation was recorded in the vicinity of an installed F404 engine at four engine conditions ranging from 50% thrust to afterburner. The Hybrid beamforming method has been used to generate equivalent source models that are then propagated outward as an approximation of the sound field. Analysis of these reconstructions reveal up to four spatiospectral lobes, phenomena seen in other high-performance aircraft. These lobes are ray traced to the jet centerline and fit parameters are extracted to determine apparent source location and radiation angle. Plotted trends show results that are qualitatively similar to those identified in previous studies [11]. It is concluded for the supersonic regimes that each lobe is the product of interactions taking place in distinct regions of the source. These are identified as being downstream of the supersonic core, between the supersonic and potential core tips, and upstream of the potential core tip. Similar behavior is also present for subsonic conditions that cannot have the same explanation due to the lack of supersonic flow structure. Impingement noise is investigated as a potential cause of Lobe 1 though this seems unlikely. In the end the underlying mechanic is still unknown.

The accuracy of the results presented in this paper are limited by the methods. Due to the spatial Nyquist frequency of the array, the Hybrid Method can only create accurate field reconstructions up to ~500 Hz, after which aliasing introduces significant error. For lobe tracking, the ray tracing method used here struggles to distinguish two closely overlapping lobes. Additionally, local maxima do not always fall directly on a lobe, thus least means square fitting sometimes results in a line that does not perfectly represent the lobe. Future work will use techniques to improve on these errors. UPAINT is an interpolation method that has been shown [19] to artificially increase the spatial Nyquist frequency and thereby reduce the effects of grating lobes. Correlation analysis [4] has also been used to separate the lobes. This would allow for more reliable ray tracing and analyses of the lobes, especially at frequencies where there is significant overlap.

Acknowledgments

This work is funded by ONR grant number N00014-21-1-2069 titled "Connecting analyses of installed tactical jet engine noise with simulated and laboratory-scale data," with project monitor Dr. Steven Martens (Code 351 Jet Noise Reduction). Distribution A: Approved for public release; distribution unlimited. Cleared 05/26/20222; 43-9696-22

VI. References

[1] Martens, S., and Spyropoulos, J. T. "Practical Jet Noise Reduction for Tactical Aircraft," *Proceedings of ASME Turbo Expo 2010: Power for Land, Sea and Air,* Glasgow, Scotland Jun 14-18, 2010.

[2] Tam, C. K. W., and Golebiowski, M. "On the Two Components of Turbulent Mixing Noise from Supersonic Jets." AIAA Paper No. 96-1716, May 1996.

[3] Neilsen, T. B., Gee, K. L., Wall, A. T., James, M. M., and Atchley, A. A. "Comparison of Supersonic Full-Scale and Laboratory-Scale Jet Data and the Similarity Spectra for Turbulent Mixing Noise." *Proceedings of Meetings on Acoustics*, Vol. 19, 2013. https://doi.org/10.1121/1.4799664.

[4] Wall, A. T., Gee, K. L., Neilsen, T. B., Harker, B. M., McInerny, S. A., McKinley, R. L., and James, M. M. "Investigation of Multi-Lobed Fighter Jet Noise Sources Using Acoustical Holography and Partial Field Decomposition Methods," AIAA Paper 2015-2379, 2015.

[5] Wall, A. T., Gee, K. L., Neilsen, T. B., McKinley, R. L., and James, M. M. "Military Jet Noise Source Imaging Using Multisource Statistically Optimized Near-Field Acoustical Holography." *The Journal of the Acoustical Society of America*, Vol. 139, No. 4, 2016, pp. 1938–1950. https://doi.org/10.1121/1.4945719.

[6] Harker, B. M., Neilsen, T. B., Gee, K. L., Wall, A. T., and James, M. M. "Spatiotemporal-Correlation Analysis of Jet Noise from a High-Performance Military Aircraft," AIAA Paper 2015-2376, 2016.

[7] Wall, A. T., Leete, K. M., Gee, K. L., Neilsen, T. B., James, M. M., and McKinley, R. L. "Preliminary Investigation of Multilobe Fighter Jet Noise Sources Using Acoustical Holography," AIAA Paper 2017-3520, 2017.

[8] van Komen, D. F., Harker, B. M., Neilsen, T. B., Gee, K. L., Hales Swift, S., Wall, A. T., Micah Downing, J., and James, M. M. "Characterizing Distinct Components of Tactical Aircraft Noise Sources." *The Journal of the Acoustical Society of America*, Vol. 147, No. 5, 2020, pp. 3550–3564. https://doi.org/10.1121/10.0001260.

[9] Stout, T. A., Gee, K. L., Neilsen, T. B., Wall, A. T., and James, M. M. "Acoustic Intensity near a High-Powered Military Jet Aircraft." *The Journal of the Acoustical Society of America*, Vol. 138, No. 1, 2015, pp. EL1–EL7. https://doi.org/10.1121/1.4921746.

[10] Leete, K. M., Vaughn, A. B., Bassett, M. S., Rasband, R. D., Novakovich, D. J., Gee, K. L., Campbell, S. C., Mobley, F. S., and Wall, A. T. "Jet Noise Measurements of an Installed Ge F404 Engine," AIAA Paper 2021-1638 2021.

[11] Leete, K. M., Wall, A. T., Gee, K. L., Neilsen, T. B., James, M. M., and Downing, J. M. "Acoustical Holography-Based Analysis of Spatiospectral Lobes in High-Performance Aircraft Jet Noise." *AIAA Journal*, Vol. 59, No. 10, 2021, pp. 4166–4178. https://doi.org/10.2514/1.j059400.

[12] Seiner, J. M., Ponton, M. K., Jansen, B. J., and Lagen, N. T. "The Effects of Temperature on Supersonic Jet Noise Emission." *14th DGLR/AIAA aeroacoustics conference*, Vol. 1, 1992, pp. 295–307.

[13] Long, D. F. "Jet Noise Source Location via Acoustic Holography and Shadowgraph Imagery." *14th AIAA/CEAS Aeroacoustics Conference (29th AIAA Aeroacoustics Conference)*, AIAA paper 2008-2888. May 2008, pp. 5–7. https://doi.org/10.2514/6.2008-2888.

[14] Tam, C. K. W., and Parrish, S. A. "Noise of High-Performance Aircraft at Afterburner." *Journal of Sound and Vibration*, Vol. 352, 2015, pp. 103–128. https://doi.org/10.1016/j.jsv.2015.04.010.

[15] Liu, J., Corrigan, A., Kailasanath, K., and Taylor, B. "Impact of the Specific Heat Ratio on the Noise Generation in a High-Temperature Supersonic Jet," AIAA Paper 2016-2125, 2016.

[16] Wall, A. T., Gee, K. L., and Neilsen, T. B. "Multisource Statistically Optimized Near-Field Acoustical Holography." *The Journal of the Acoustical Society of America*, Vol. 137, No. 2, 2015, pp. 963–975. https://doi.org/10.1121/1.4906585.

[17] Vold, H., Shah, P., Morrisz, P., Du, Y., and Papamoschou, D. "Axisymmetry and Azimuthal Modes in Jet Noise," AIAA Paper 2012-2214, 2012.

[18] Michel, U. "History of acoustic beamforming," 1st Berlin Beamforming Conference, BEBEC, Berlin, 2006.

[19] Harker, B. M., Gee, K. L., Neilsen, T. B., Wall, A. T., and James, M. M. "Source Characterization of Full-Scale Tactical Jet Noise from Phased-Array Measurements." *The Journal of the Acoustical Society of America*, Vol. 146, No. 1, 2019, pp. 665–680. https://doi.org/10.1121/1.5118239.

[20] Stout, T. A., Gee, K. L., Neilsen, T. B., Wall, A. T., and James, M. M. "Source Characterization of Full-Scale Jet Noise Using Acoustic Intensity," *Noise Control Engineering Journal,* Vol. 63, 2015.

[21] Harker, B. M., Gee, K. L., Neilsen, T. B., Wall, A. T., and James, M. M. "Beamforming-Based Wavepacket Model for Noise Environment Predictions of Tactical Aircraft," AIAA Paper 2017-4048, 2017.

[22] Padois, T., Gauthier, P. A., and Berry, A. "Inverse Problem with Beamforming Regularization Matrix Applied to Sound Source Localization in Closed Wind-Tunnel Using Microphone Array." *Journal of Sound and Vibration*, Vol. 333, No. 25, 2014, pp. 6858–6868. https://doi.org/10.1016/j.jsv.2014.07.028.

[23] Padois, T., Berry, A., Gauthier, P. A., and Joshi, N. "Beamforming Matrix Regularization and Inverse Problem for Sound Source Localization: Application to Aero-Engine Noise," AIAA Paper 2013-2212, 2013.

[24] Swift, S. H., Gee, K. L., Neilsen, T. B., Wall, A. T., Downing, J. M., and James, M. M. "Spatiotemporal Correlation Analysis of Jet Noise from a Round-Nozzle Supersonic Aircraft." AIAA Paper 2018-3938, 2018.

[25] Leete, K. M., Gee, K. L., Liu, J., and Wall, A. T. "Coherence Analysis of the Noise from a Simulated Highly Heated Laboratory-Scale Jet." *AIAA Journal*, Vol. 58, No. 8, 2020, pp. 3426–3435. https://doi.org/10.2514/1.j059112.

[26] Liu, J., Kailasanath, K., and Gutmark, E. J. "Similarity Spectra Analysis in Highly Heated Supersonic Jets Using Large-Eddy Simulations," AIAA Paper 2017-0926, 2017.

[27] Liu, J., Corrigan, A., Kailasanath, K., and Gutmark, E. "Impact of Chevrons on Noise Source Characteristics in Imperfectly Expanded Jet Flows," AIAA Paper 2015-2835, June 2015.

[28] Mathews, L. T., Gee, K. L., Leete, K. M., and Wall, A. T. "Acoustic Source Characterization of an Installed GE F404 Engine Using Near-Field Acoustical Holography." *28th AIAA/CEAS Aeroacoustics Conference*. (submitted)

[29] Potter, R. C. “An Investigation to Locate the Acoustic Sources in a High Speed Jet Exhaust Stream,”, Technical report WR 68-4, 1968.

[30] Vaughn, A. B., Gee, K. L., Swift, S. H., Leete, K. M., Wall, A. T., Downing, J. M., and James, M. M. “Source Localization of Crackle-Related Events in Military Aircraft Jet Noise.” AIAA Paper *AIAA Journal*, Vol. 59, No. 6, 2021, pp. 2251–2261. https://doi.org/10.2514/1.j059823.

[31] Christian, M. A., Mathews, L. T., Gee, L. L., Streeter, J., Wall, A., Johnson, J. P., and Campbell, S. C. “Installed F404 Engine Noise Source Characteristics from Far-Field Directivity Measurements.” *28th AIAA/CEAS Aeroacoustics Conference*. (submitted)